materials

MDPI

Article

Effects of Substitution and Substrate Strain on the Structure and Properties of Orthorhombic $Eu_{1-x}Y_xMnO_3$ ($0 \leq x \leq 0.5$) Thin Films

Yonny Romaguera-Barcelay [1,2,*], Fábio Gabriel Figueiras [3], Ernesto Govea-Alcaide [2], Walter Ricardo Brito [4], Henrique Duarte da Fonseca Filho [5], Ariamna María Dip Gandarilla [4], Ştefan Ţălu [6,*], Pedro B. Tavares [7] and Javier Pérez de la Cruz [8]

1 BioMark@UC, Faculty of Sciences and Technology, University of Coimbra, 3004-531 Coimbra, Portugal
2 Department of Physics, Federal University of Amazonas, Manaus 69067-005, AM, Brazil; egoveaalcaide@gmail.com
3 IFIMUP & Departamento de Física e Astronomia da Faculdade de Ciências da Universidade do Porto, 4169-007 Porto, Portugal; fabio.figueiras@fc.up.pt
4 Laboratorio de Bioeletrônica e Eletroanalítica (LABEL), Department of Chemistry, Federal University of Amazonas, Manaus 69067-005, AM, Brazil; wrbrito@ufam.edu.br (W.R.B.); ariamna@ufam.edu.br (A.M.D.G.)
5 Laboratory of Synthesis of Nanomaterials and Nanoscopy, Physics Department, Federal University of Amazonas-UFAM, Manaus 69067-005, AM, Brazil; hdffilho@ufam.edu.br
6 The Directorate of Research, Development and Innovation Management (DMCDI), The Technical University of Cluj-Napoca, 400020 Cluj-Napoca, Romania
7 Centro de Química-Vila Real, Departamento de Química, ECVA, Universidade de Trás os Montes e Alto Douro, 5000-801 Vila Real, Portugal; ptavares@utad.pt
8 ISQ-Instituto de Soldadura e Qualidade, 2740-120 Porto Salvo, Portugal; jpcruz@isq.pt
* Correspondence: yonny.barcelay@uc.pt (Y.R.-B.); stefan.talu@auto.utcluj.ro (Ş.Ţ.)

check for updates

Citation: Romaguera-Barcelay, Y.; Figueiras, F.G.; Govea-Alcaide, E.; Brito, W.R.; Filho, H.D.d.F.; Gandarilla, A.M.D.; Ţălu, Ş.; Tavares, P.B.; de la Cruz, J.P. Effects of Substitution and Substrate Strain on the Structure and Properties of Orthorhombic $Eu_{1-x}Y_xMnO_3$ ($0 \leq x \leq 0.5$) Thin Films. *Materials* **2023**, *16*, 4553. https://doi.org/10.3390/ma16134553

Academic Editor: Lucia Del Bianco

Received: 27 May 2023
Revised: 19 June 2023
Accepted: 20 June 2023
Published: 23 June 2023

Copyright: © 2023 by the authors. Licensee MDPI, Basel, Switzerland. This article is an open access article distributed under the terms and conditions of the Creative Commons Attribution (CC BY) license (https://creativecommons.org/licenses/by/4.0/).

Highlights:

- Orthorhombic $Eu_{1-x}Y_xMnO_3$ ($0.0 \leq x \leq 0.5$) thin films were successfully synthesized by spin-coating.
- The film phase evidences an additional contribution to lattice strain with increasing Y-content.
- Appreciable modification of magnetic response from bulks to films due to structural distortions.

Abstract: The effects on the structure and magnetic properties of $Eu_{1-x}Y_xMnO_3$ ($0.0 \leq x \leq 0.5$) thin films due to lattice strain were investigated and compared with those obtained in equivalent composition ceramics. The films were deposited by spin-coating chemical solution onto Pt\$TiO_2$\$SiO_2$\Si (100) standard substrates. X-ray diffraction and Raman spectroscopy measurements revealed that all films crystallize in orthorhombic structure with space group *Pnma*, observing an added contraction of the unit cell with increasing Y-substitution ou Eu, corresponding to a broadening of the Mn-O1-Mn angle and a gradual decrease in magnetic order response.

Keywords: $Eu_{1-x}Y_xMnO_3$; manganites; spin-coating; thin films

1. Introduction

Transition metal oxides have many fascinating physical properties, such as high temperature, superconductivity, piezoelectricity, ferroelectricity, magnetism, and multiferroicity. Hence, these materials are still objects of intense scientific, engineering, and economic interest, considering the extensive technological applications already in use and further yet to be discovered. Rare-earth manganites $RMnO_3$ are among some of the most relevant functional oxide materials, mainly due to intrinsic strong correlated electron mechanisms, leading to exhibiting structural-orbital-magnetic-electric coupling effects. In particular, it can be used for barriers and interfaces in controlled spin transport devices [1–6]. According to the

ionic radius of rare earth elements, the manganites can exhibit two main distinct structural symmetries. The perovskite-like orthorhombic phase, comprising a network of octahedral MnO_6 building blocks, surrounds relatively larger R^{3+} cations from La to Dy. In particular, systems like $GdMnO_3$, $TbMnO_3$, and $DyMnO_3$ reveal magnetoelectric properties owed to competitive ferromagnetic (FM) and antiferromagnetic (AFM) exchanges. In such cases, the Mn-O1-Mn angle is considered the primary order parameter to understand the modulated spin-lattice coupling mediated ferroelectric (FE) ground states [7,8]. The hexagonal space group can be found in the $RMnO_3$ systems of smaller R^{3+} cations, including Lu, Y, and Sc [9–14]. These compounds are based on MnO_5 layers and present only AFM order at low temperatures due to weak spin-orbit coupling (<90 K). Nonetheless, the FE order prevails up to substantial high temperatures. In addition to ionic displacements in these systems, other complex mechanisms related to exchange effects of electron orbital polarization contribute to the ferroelectric state [15–18]. In this particular case, the $Eu_{1-x}Y_xMnO_3$ system can exhibit both the orthorhombic ($x \leq 0.5$) and hexagonal phase ($x > 0.5$), allowing the possibility of tuning the magnetic and polar phases through manipulation of the A-site size, the partial substitution of larger Eu^{3+} ions for smaller isovalent Y^{3+} ions without increasing the *R*-site magnetic complexity. The variation of the Mn-O1-Mn bond angle in these systems is also associated with the development of complex magnetic states and ferroelectric phases, leading to the magnetoelectric properties exhibited by this system [19–21]. The $Eu_{1-x}Y_xMnO_3$ compound shows the characteristics of a paramagnetic to an incommensurate antiferromagnetic phase (AFM-1) at *Néel* temperature (T_N), varying monotonously from 52−45 K ($x = 0$) to 45 K ($x = 0.50$) [7,22]. For $x < 0.1$, a transition from the AFM-1 to a canted A-type antiferromagnetic phase occurs at 43 K ($x = 0$) to 33 K ($x = 0.1$) [22]; next while it emerges for $x < 0.25$ [23]. For the compositions $0.25 < x < 0.35$, a cycloidal modulated antiferromagnetic and ferroelectric phase (AFM-2) becomes apparent. For $0.35 < x < 0.55$, a re-entrant magnetic phase, corresponding to two successive magnetic transitions, is associated with the cycloidal plane's rotation from the ab to the bc plane [7,22,23]. This rotation implies that the spontaneous electric polarization changes from the *c*-axis to the *a*-axis [23]. Other authors consider, for $0.15 < x < 0.35$, a further low temperature modulated conical magnetic and ferroelectric phase (AFM-3) [7,22–24]. However, the magnetic structure of low-temperature phases continues to be intensely studied. Besides the studies of $Eu_{1-x}Y_xMnO_3$ as single crystals and conventional ceramics [22], it becomes relevant to investigate this system in the form of thin films since the properties may differ from those of bulk ceramics due to the influence of dimensional strain and the substrate interface. Even with their granular nature, thin films have attracted great interest and require a systematic comparison between the behavior of single crystals and ceramics [22,25,26]. In addition to contributing to extend the understanding and enhancing the underlying multiferroic mechanisms, thin film materials are crucial for developing potential applications and further fabrication of functional electro-optical devices. Chemical solution deposition methods like the sol-gel spin-coating technique provide higher composition control, lower processing temperatures, shorter fabrication time, and relatively low cost, compared to other chemical and physical vapor deposition thin-film-forming processes such as evaporation, pulsed laser, and sputtering [27].

As thin films can be subjected to strong elastic strains due to structural mismatch with respect to substrates, their intrinsic physical properties can be actively modified. These effects are under study on other strained perovskite thin films, which in bulk form exhibit orthorhombic structures: $EuMnO_3$, $GdMnO_3$, $LaMnO_3$, $DyMnO_3$, $YMnO_3$, etc. [6,27]. From this perspective, the main objective of this work is to analyze and determine the effects of Y substitution of Eu and substrate strain on the structural and magnetic properties of orthorhombic $Eu_{1-x}Y_xMnO_3$ thin films and, in particular, thin film oxides prepared by the sol-gel spin-coating method, taking into consideration some practical technical factors, including low production cost, equipment versatility, simplicity of preparation, composition control, and low sintering temperature. The experimental results encompassing crystal

structure, dynamics, and the magnetic properties of these thin films are further compared with bulk ceramic samples of equivalent nominal composition (x = 0; 0.1; 0.2; 0.3; 0.4; 0.5).

2. Experimental Procedure

The studied $Eu_{1-x}Y_xMnO_3$ thin films were prepared by a sol-gel method using standard Pt\$TiO_2$\$SiO_2$\Si (100) wafers as substrates. Details of precursor solutions and film preparation are available in refs. [27,28]. Thermogravimetric (TG) and differential thermogravimetric analyses (DTA) were conducted in the $Eu_{1-x}Y_xMnO_3$ precursor solutions using a *Seteram Labsys* TG–DTA/DSC analyzer; each solution was previously dried at 100 °C for 48 h, forming the so-called dry solution. Afterward, it was heated in an air atmosphere at 10 °C/min from room temperature up to 1000 °C. The structural characterization of the films was carried out with a *PANalytical MRD* diffractometer, equipped with an *X'Celerator* detector in *Bragg-Brentano* geometry, using a Cu Kα radiation (λ = 1.5418 Å) source, a step of 0.017°/100 s from 20° up to 80° (2θ). Unpolarized micro-Raman spectroscopy was performed at ambient conditions for the 200–800 cm^{-1} spectral range, using a 514.5 nm Argon laser line as the excitation source. The incident power was kept below 10 mW to avoid local sample heating. The scattered light was analyzed by a *T64000 Jobin-Yvon* triple spectrometer, operating in triple subtractive mode and equipped with a liquid-nitrogen-cooled charge-coupled device. The spectral slit width was ~1.5 cm^{-1}. The parameters of the observed Raman modes (frequency, line width, and amplitude) were calculated using *IgorPro* software 6.0 from the best fit of a sum of damped oscillator functions [25]. Samples magnetization was measured using a *Quantum Design* SQUID magnetometer in reciprocating sample option (RSO) mode with a sensitivity of ~10^{-7} emu. Measurements were carried out in a heating run from 5 to 300 K following protocols of zero field-cooled (ZFC) and field-cooled (FC) at 100 Oe. The experimental and calculated data were processed according to the error analysis procedures, accounting the intrinsic precision of the methods and corrections derived from the formulas used [29].

3. Results and Discussion

3.1. C.1. Phase Formation

Figure 1a,b shows the TG–DTA curves of the precursor solutions comprising the nominal concentrations of $|Eu| = 1 - x$; $|Y| = x$; in relation to $|Mn| \equiv 1$ cation.

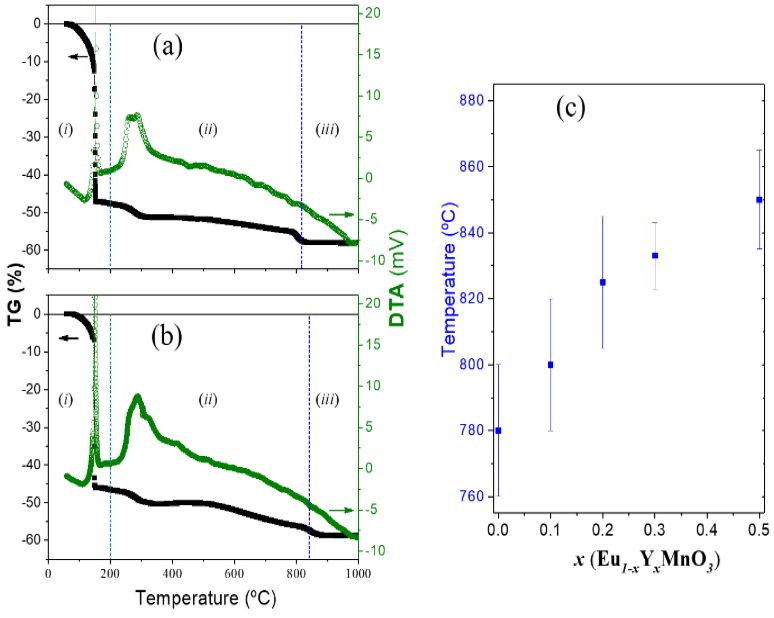

Figure 1. Thermal decomposition curves of the $Eu_{1-x}Y_xMnO_3$ precursors solutions for x = (**a**) 0.2; and (**b**) 0.5. (**c**) Perovskite phase formation temperature for $Eu_{1-x}Y_xMnO_3$ thin films.

The decomposition process includes three main steps: (*i*) solvent evaporation and (*ii*) calcination and pre-oxidation of precursor cations; these two preparation steps are similar to the ones reported for other oxide films [27,28]. The third step (*iii*) is the most important since it evolves the formation of the intended crystalline phase. The TG–DTA curves profiles, steps, and temperature intervals, obtained during the decomposition of each precursor solution exhibit slight variations depending on the ratio of substitution elements used. Overall, the formation of the $Eu_{1-x}Y_xMnO_3$ perovskite crystalline phase is indicated by the precursor's loss weight rate stabilizing beyond 770–880 °C. As seen in Figure 1c, the temperature threshold for the phase formation increases gradually with Y substitution (x) in relation to the $EuMnO_3$ film. Consequently, the final sintering treatment was set at 800 °C for the x = 0 up to 850 °C for x = 0.5.

3.2. C.2. Surface Morphology

Representative SEM images of the $Eu_{1-x}Y_xMnO_3$ films surface view and respective cross-section backscattering are shown in Figure 2a–d. Generally, each film exhibits a homogeneous crystallite size and a consistent dissemination of cracks throughout all surfaces.

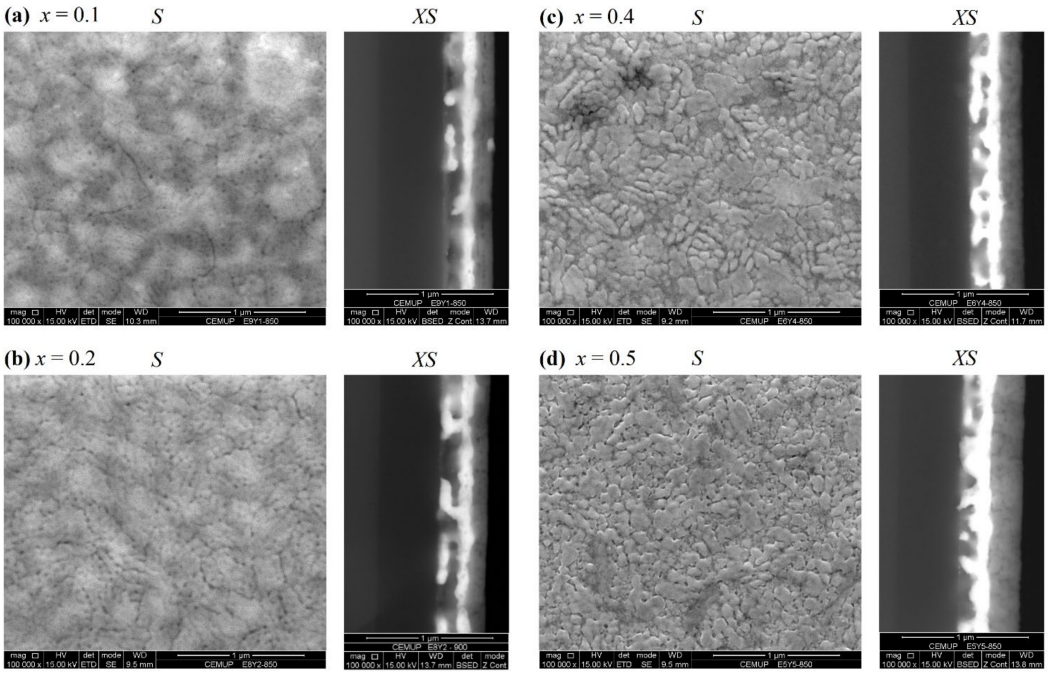

Figure 2. $Eu_{1-x}Y_xMnO_3$ thin films representative SEM images obtained at $\times 10^5$ magnification, for, x = (**a**) 0.1; (**b**) 0.2; (**c**) 0.4; (**d**) 0.5, respective surface (left) and cross-section (right).

As the content of Y^{3+} substitution increases, the average grain (crystallite) size and average area enclosed by cracks (agglomerates) decreases, whereas the film thickness gradually increases. A summary of the results extracted from these images is displayed in Table 1.

Table 1. Topographic parameters calculated from SEM images of $Eu_{1-x}Y_xMnO_3$ thin films. <*grain*>: average grain size ± 10%; <*aggl.*>: agglomerate size ± 10%; <*t*>: thickness ± 10%.

x (%)	<*grain*> (nm)	<*aggl.*> (nm)	<*t*> (nm)
0.1	220	525	140
0.2	90	275	160
0.3	50	145	180
0.4	50	105	200
0.5	40	80	250

3.3. C.3. Crystal Structure

Figure 3 presents the grazing angle X-ray diffraction (GA-XRD) patterns obtained at ambient conditions from the series of $Eu_{1-x}Y_xMnO_3$ thin films, where the diffraction peaks resultant from the substrate are labeled with (∗) symbols.

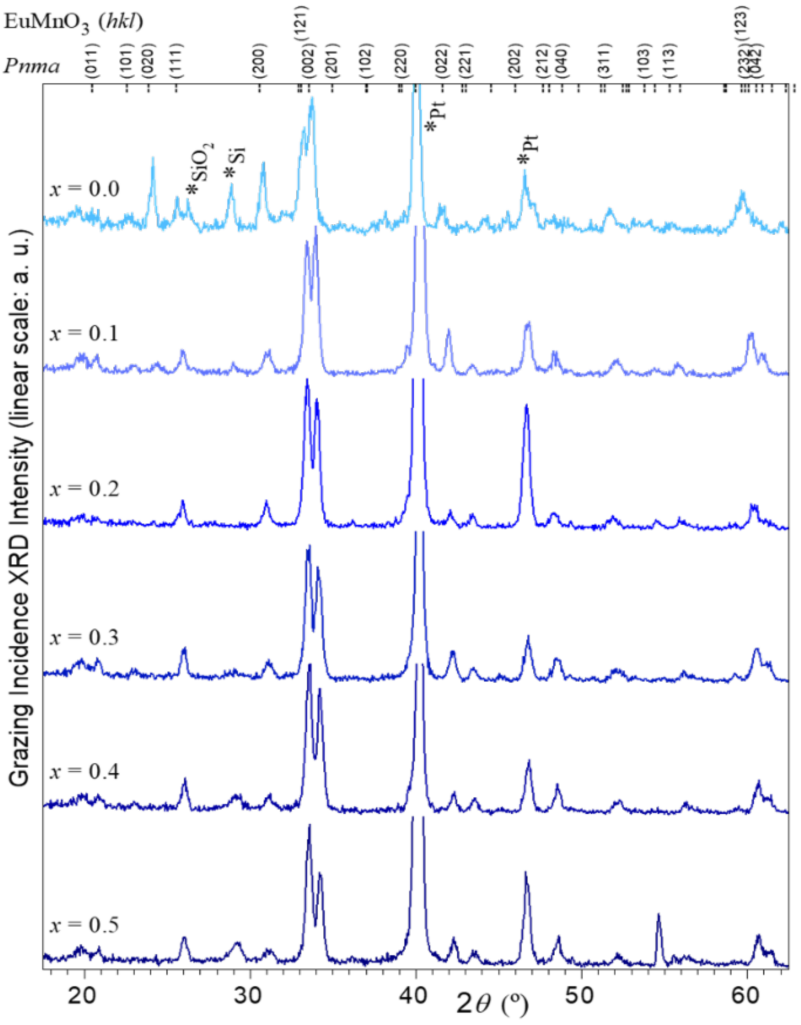

Figure 3. Spectra of X-ray diffraction on grazing angle of $Eu_{1-x}Y_xMnO_3$ thin films with $0 \leq x \leq 0.5$ concentration. The Bragg reflections belonging to the $EuMnO_3$ ($x = 0$) phase are identified with Miller indexes. (*) Diffraction peaks of the substrate.

Thin films with composition $0 \leq x \leq 0.5$ exhibit a typical XRD diffractogram profile associated with the *Pnma* (62) symmetry group, as observed in analogous bulk samples [22,25,26]. Likewise, no relevant secondary phases were detected. On the other hand, films with $x \geq 0.6$ revealed concomitance of hexagonal and perovskite phases and are not the object of the present study since it is not viable to evaluate a direct correlation to each phase and its composition. A control film of $YMnO_3$ ($x = 1.0$), synthesized by the same spin-coating sol-gel method and sintered at 850 °C, confirms the dominance of $P6_3cm$ symmetry [28,30,31]. Overall comparison of the graphs enables us to observe a shift of reflection peaks towards higher angles as x increases, suggesting a relative contraction of the unit cell volume. In the diffractogram of film $EuMnO_3$ ($x = 0.0$) and to a lesser degree in film $Eu_{0.9}Y_{0.1}MnO_3$ ($x = 0.1$), it is possible to discern that the intensity of the reflection peak at $2\theta \sim 24°$, indexed to planes (020) of orthorhombic phase, are over-proportional to the spectra expected from a random polycrystalline film. This specific feature, not detected on the other film diffractograms, is suggestive that the films with $x = 0.0$ and 0.1 can have partially grown with a preferred orientation along the *b*-axis. For

x > 0.1, the films XRD do not show signs of oriented growth and are assumed to be dominated by polycrystalline form.

Detailed (*Le Bail*) analysis of the diffractograms enables calculating the respective thin films lattice parameters. The fitting model used in the indexation to the *Pnma* space group and conventional *pseudo-Voigt* function to describe the peak shape [25]. Figure 4a plots the dependence of the pseudo-cubic ($_{pc}$) lattice parameters defined as $a_{pc} = a/\sqrt{2}$, $b_{pc} = b/2$, and $c_{pc} = c/\sqrt{2}$ with *x*-composition, where *a*, *b*, and *c* are the conventional orthorhombic *Pnma* lattice parameters.

The relation $a_{pc} > c_{pc} > b_{pc}$ is fulfilled for all compounds characteristic of the designated *O′* structure, typically found in rare-earth manganites. In this *O′* structure, the octahedral MnO_6 frames are associated with a strong *Jahn-Teller* distortion and orbital ordering [32]. While in bulk ceramics, a linear decrease of lattice volume is observed in direct correlation with the cube of the effective A-site radius [25,26], it is evident that the series of films' pseudo-cubic lattice parameters gradually decrease with increasing Y-substitution content in the range 0.0 to 0.5.

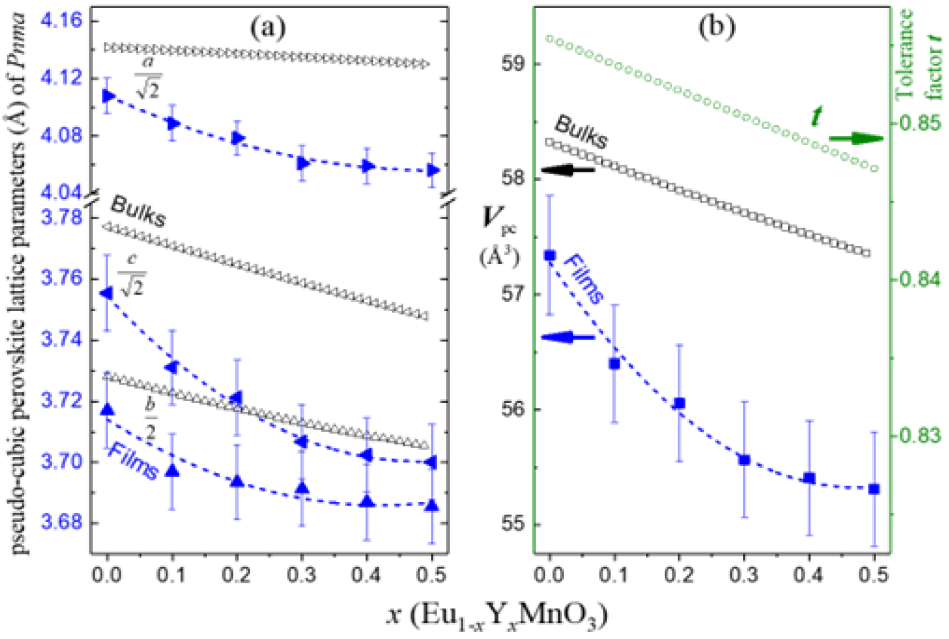

Figure 4. Dependence of the pseudo-cubic lattice parameters with *x* of the $Eu_{1-x}Y_xMnO_3$ thin films (solid symbols) and ceramics [33] (respective open symbols). (**a**) (►) a_{pc}, (▲) b_{pc}, and (◄) c_{pc} where dashed lines correspond to respective quadratic degree polynomial function best fit to experimental results. (**b**) Calculated lattice volume V_{pc} of (■) films, (□) bulks, and comparison to the theoretical tolerance factor (○) *t*.

Table 2 resumes the values of quadratic $|\Delta^2 y/\Delta x^2|$ and linear $|\Delta y/\Delta x|$ slopes obtained from best fitted quadratic degree polynomial functions ($y = |\Delta^2 y/\Delta x^2| \cdot x^2 + |\Delta y/\Delta x| \cdot x + y_0$).

Table 2. Slope values (in Å) degree 2 polynomial fit of the lattice parameter for $Eu_{1-x}Y_xMnO_3$ thin films. The values obtained for ceramic samples of the same compound are extracted from Ref. [24].

Sample	***a***		***b***		***c***		***V***	
Type	$\Delta a/\Delta x$	$\Delta^2 a/\Delta x^2$	$\Delta b/\Delta x$	$\Delta^2 b/\Delta x^2$	$\Delta c/\Delta x$	$\Delta^2 c/\Delta x^2$	$\Delta V/\Delta x$	$\Delta^2 V/\Delta x^2$
Ceramics [26]	−0.020 ± 0.03	0.007 ± 0.06	−0.058 ± 0.003	0.022 ± 0.006	−0.064 ± 0.002	0.008 ± 0.004	−2.169 ± 0.45	0.386 ± 0.86
Thin films series	−0.206 ± 0.03	0.204 ± 0.05	−0.134 ± 0.03	0.159 ± 0.07	−0.226 ± 0.02	0.236 ± 0.04	$-8.330^{\pm 0.88}$	8.88 ± 1.70

Analogously to $Eu_{1-x}Y_xMnO_3$ ceramics, the lattice compression, due to Y^{3+} substitution, occurs in all axes, more manifested in *c*- and *b*- and less in *a*- directions. The quadratic terms $|\Delta^2 y/\Delta x^2|$ are residual, and the pseudo-cubic lattice parameters follow a straight linear slope with the relation $|\Delta a/\Delta x| < |\Delta b/\Delta x| \leq |\Delta c/\Delta x|$ [33], which can be traced directly to the system tolerance factor ($t = \langle(1 - x)\cdot r_{Eu} + x\cdot r_Y + r_O\rangle/\sqrt{2}\cdot\langle r_{Mn} + r_O\rangle$). Quite differently from the described linear behavior reported for the ceramic series, the contraction of lattice parameters in the series of $Eu_{1-x}Y_xMnO_3$ thin films follow a non-linear correlation to *t*. The results indicate an additional compression mechanism at play, patently due to the strain in the film phase induced by the substrate effect. Figure 4a,b expose the film lattice strain by separating it from the corresponding linear behavior found on bulks. The film lattice contractions are more relevant and evenly distributed in the basal plane *a*- and *c*- directions ($< -0.5\%$ to -1.7%) than in the *b*-direction ($\sim -0.5\%$). This conjugation can explain why it is possible to advocate partial preferential growth of the film phase with $x = 0$ compatible with a less strained *b*-axis. On films, the relations become $|\Delta a/\Delta x| \approx |\Delta c/\Delta x| > |\Delta b/\Delta x|$, respectively, ~10, ~3.5, and ~2 times larger than reported for ceramics. Moreover, the quadratic terms have a similar magnitude to the linear ones and follow the same distribution $|\Delta^2 a/\Delta x^2| \approx |\Delta c^2/\Delta x^2| > |\Delta b^2/\Delta x^2|$. Subsequently, the continuous reduction of the unit cell parameters and volume attests that the systems remain in the original *Pnma* phase, suggesting a supplementary adjustment of MnO_6 octahedra distortions and tilting [34]. The lattice volume contraction is near -1.7% for $x = 0$ and reaches a maximum of -3.7% for $x \geq 0.3$.

3.4. C.4. Raman Spectroscopy

Figure 5 shows the unpolarized Raman spectra obtained from the series of $Eu_{1-x}Y_xMnO_3$ thin films recorded at ambient conditions.

Due to the main contribution of a polycrystalline phase in the series of samples, the experimental spectra simultaneously exhibited all Raman-active modes A_g, B_{1g}, B_{2g}, and B_{3g}; the assignment [13,35,36] assumes the band at ~359 cm^{-1} is resulting from the bending or tilt (T) mode of the MnO_6 octahedra, which is activated by the (101) rotations (symmetry A_g); the band at ~478 cm^{-1} is assigned to a *Jahn-Teller* type asymmetric stretching (AS) mode also involving the O(II) atoms (symmetry A_g); the band at ~498 cm^{-1} is assigned to a bending mode (B) (symmetry B_{2g}); and the band at ~612 cm^{-1} is associated to a symmetric stretching mode (SS) involving the O(II) atoms (symmetry B_{2g}). These modes can be detected in the range from 350 to 650 cm^{-1} and are also signaled in ceramic samples [25,35,36], corroborating the *Pnma* symmetry of the films already ascertained from the XRD data.

In the Raman spectrum of the $Eu_{1-x}Y_xMnO_3$, thin films with $x = 0$ and 0.1 are observed as additional modes at ~220 and ~685 cm^{-1}; these can be interpreted as a Raman activation of active infrared modes—a direct consequence of the lattice distortions occurring in thin films due to the lattice mismatch between film and substrate and the film-substrate interaction [32], consistent with the partial presence of an orientated layer as mentioned from the XRD analysis. In samples with $0.2 \leq x \leq 0.5$, the contribution of an orientated layer is not so significant. Hence, the mode at ~220 cm^{-1} vanished, while the broad shoulder band above ~620 cm^{-1} can still be attributed to distortions in the film lattice induced by the substrate effect. Still, due to the dominant polycrystalline structure, these distortions are disordered and relaxing through the film thickness, contributing to the convolution of peaks deriving from a distribution of modes.

Figure 5 shows the dependence in *x* of the peak center position wave number (ω) of the four most intense Raman modes assigned T, AS, B, and SS, measured in the films and compared to the ceramics with matching composition [25]. These modes are particularly interesting because they indicate the structural deformations in the $Eu_{1-x}Y_xMnO_3$ thin films. For the thin films, the wave number of the tilt mode (T) increases linearly with Y^{3+} content with a slope $\Delta\omega^T/\Delta x$ films = 50 ± 2 cm^{-1}, a similar linear behavior $\Delta\omega^T/\Delta x$ bulks = 29 ± 2 cm^{-1} is found for the ceramic's samples [25]. Iliev et al. [35] demonstrated that such out-of-phase rotation mode and the tilt angle (θ^T) exhibit a linear behavior with slope $\Delta\omega^T/\Delta x$ = 23.5 cm^{-1}. By combining the above results, a variation of the rotation

mode and the tilt angle with x can be obtained, for the series of $Eu_{1-x}Y_xMnO_3$ thin films, of $\Delta\theta^T/\Delta x = 2.1°$. This value indicates that the volume reduction, anticipated from X-ray diffraction analysis, corresponds to an increase in the tilt angle with up to $x = 0.5$, close to 1°. While in Y-doped ceramics, the variation was $\Delta\theta/\Delta x = 1.3°$, representing an increase in the tilt angle of only 0.05° [25]. The symmetric stretching mode SS follows a near analogous constant ($\Delta\omega^{SS} \sim 2$ cm^{-1}) behavior for films and ceramics, suggesting minor variations of Mn-O_2 bond lengths with increasing x. However, in the same concentration range, the wave numbers measured for the thin films of the *Jahn-Teller* type asymmetric stretching mode (AS) and bending mode (B) exhibit a step-like discrepancy relative to the near linear $\Delta\omega/\Delta x$ behavior identified in ceramics. In effect, specifically between $x = 0.2$ and 0.3, where the four mode defined curves intersect, the pseudo-perovskite lattice c_{pc} (films) and b_{pc} (bulks) lengths coincide, as can be seen in Figure 4a.

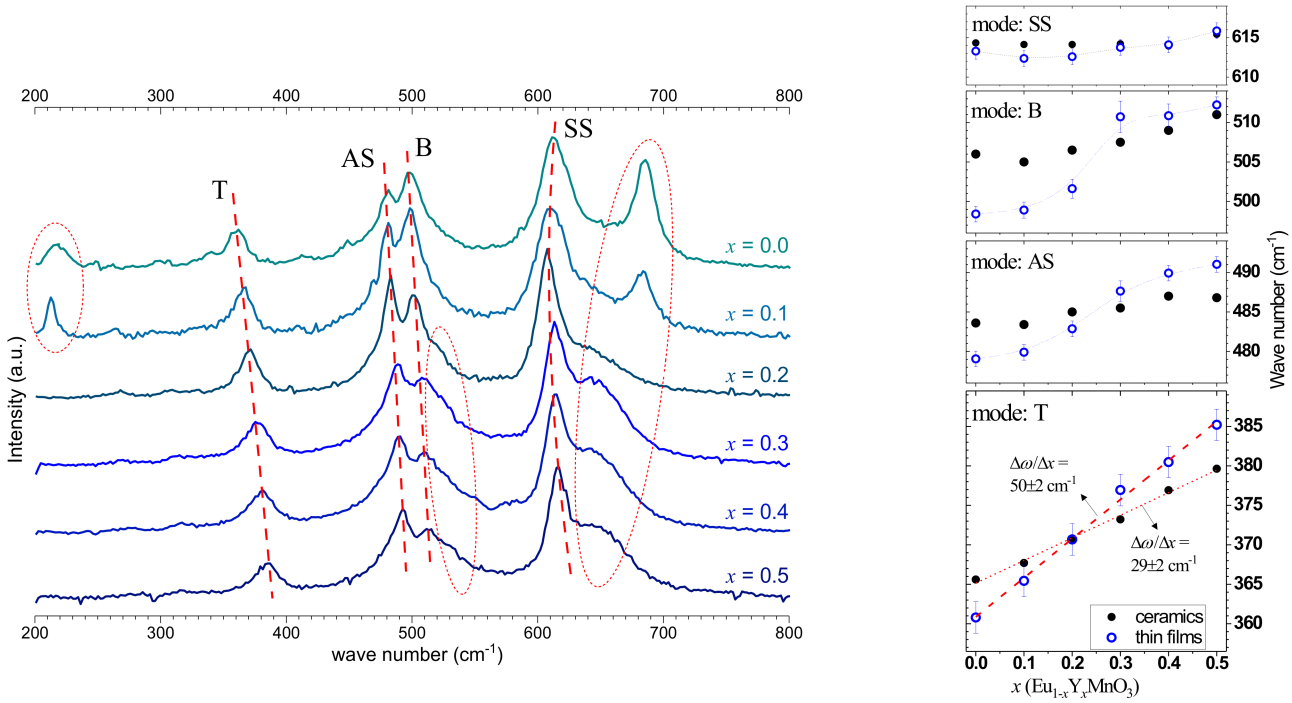

Figure 5. Un-polarized Raman spectra of $Eu_{1-x}Y_xMnO_3$ for $0 \leq x \leq 0.5$ thin films annealed at 850 °C. Mode assignment: T—tilt mode of the MnO_6 octahedra (symmetry A_g); SS—symmetric stretching mode (symmetry B_{2g}); B—bending mode (symmetry B_{2g}), and AS—*Jahn-Teller* type asymmetric stretching mode (symmetry A_g). Dashed red lines are eyes-guides for the indicated modes identification. Insets: detailed graphs of the T; AS; B; and SS modes dependence with x in the $Eu_{1-x}Y_xMnO_3$ thin films and ceramics [24].

3.5. C.5. Magnetic Properties

The structural distortions associated with the film phase and Y^{3+} substitution are expected to significantly influence the magnetic properties of the studied samples, particularly the competitive ferromagnetic (FM) and antiferromagnetic (AFM) exchange interactions. Figure 6 presents the ZFC/FC magnetization measurements performed on the $Eu_{1-x}Y_xMnO_3$ thin films from $x = 0.0$ to 0.4.

In overview, the experimental data follow a similar behavior to the ones reported in single crystal and ceramic samples of the equivalent compounds [22,25]. The difference between FC and ZFC magnetization ΔM (5 K) = M_{FC} (5 K)—M_{ZFC} (5 K) is 27.9 emu/cm^3 for $x = 0.0$, but ensuing films $0.1 \leq x \leq 0.4$ ΔM (5 K) yield, respectively, only 0.67; 0.36, 0.07; and 0.08 emu/cm^3. In $EuMnO_3$ and $Eu_{0.9}Y_{0.1}MnO_3$ films, an expected irreversibility behavior is observed for temperatures up to $T_N \sim 50$ K. Below this temperature, the characteristic weak FM arising from the canted A-type AFM was exhibited similar to $EuMnO_3$ single crystals

and ceramics samples [22,37]. However, in films with Y^{3+} concentrations ranging from 0.2 to 0.4, the irreversibility behavior persists at higher temperatures, making the precise determination of T_N difficult. The relative difference between FC and ZFC magnetization curves decreases with increasing Y^{3+} concentration, and the concavity of the FC curves inflect downward for $x \geq 0.3$, as seen in Figure 6. It is reasonable to interpret the reduction of the induced magnetic moments in $Eu_{1-x}Y_xMnO_3$ thin films with increasing x as a consequence of the volume contraction of the unit cell and the increase in the Mn-O1-Mn bond angle. While in films with x = 0.0 and 0.1, the weak FM stems from the canted A-type AFM, the incommensurate AFM for Y^{3+} concentration in the range from 0.2 to 0.4 may not be assessed as the cause of the irreversibility at temperatures above T_N. In this case, the film-substrate interface may emulate an apparently emergent FM response caused by pinning local magnetic moments induced by the excitation magnetic field [38]. This weak FM character, prolonging above 100 K, hinders the application of a Curie-Weiss model [6]. The previous results agree with those reported in Lu-doped $EuMnO_3$ thin films [17,39]; however, irreversibility behavior seems more marked in these samples.

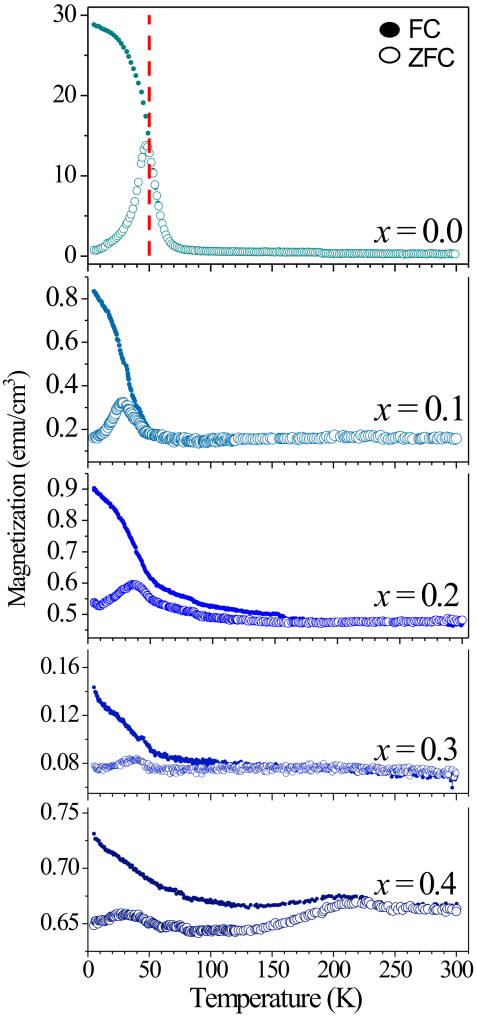

Figure 6. ZFC (open dots) and FC (closed dots) magnetization as a function of temperature for the $Eu_{1-x}Y_xMnO_3$ thin films for $0 \leq x \leq 0.4$.

4. Conclusions

Thin films of $Eu_{1-x}Y_xMnO_3$ ($0 \leq x \leq 0.5$) were successfully prepared from the precursor solutions and deposited onto $Pt\backslash TiO_2\backslash SiO_2\backslash Si$ (100) substrates. The X-ray diffraction analysis reveals that the films stabilize in a single *Pnma* orthorhombic phase up to x = 0.5,

while further substitution results in phases concomitance or full crystallization for $x = 1.0$ on $P6_3cm$ hexagonal structure. Compared to equivalent orthorhombic $Eu_{1-x}Y_xMnO_3$ bulk ceramics, the thin films revealed an enhanced decrease in unit cell volume with increasing substitution concentration, and a further increase in the inclination of the MnO_6 octahedra was ascertained by Raman spectroscopy. In contrast to ceramics samples, the films significantly smeared out the paramagnetic-canted A-type AFM transition. A weak ferromagnetic character was detected even above 100 K and attributed to the pinning of local magnetic moments at the film/substrate interface. These results corroborate the pertinence of the substrate-induced strain to modify and tune the distortions of the compound crystal lattice and ferroic properties.

Author Contributions: Conceptualization, methodology, and data collecting/analysis, writing—original draft: Y.R.-B. and J.P.d.l.C.; methodology, investigation: F.G.F., E.G.-A., H.D.d.F.F., A.M.D.G. and J.P.d.l.C.; formal analysis, methodology, resources: Y.R.-B., E.G.-A., W.R.B. and P.B.T.; writing—original draft preparation: Y.R.-B., Ș.Ț., E.G.-A. and A.M.D.G.; writing—review and editing: Y.R.-B., F.G.F., Ș.Ț. and H.D.F.F.; visualization, formal analysis, investigation, supervision: Y.R.-B., F.G.F., W.R.B. and J.P.d.l.C.; funding acquisition: W.R.B., Ș.Ț., H.D.d.F.F. and P.B.T.; conceptualization, formal analysis, investigation, methodology, project administration, resources, supervision, visualization, writing—original draft, writing—review and editing: Y.R.-B. All authors have read and agreed to the published version of the manuscript.

Funding: This research received no external funding.

Institutional Review Board Statement: Not applicable.

Informed Consent Statement: Not applicable.

Data Availability Statement: The data used to support the findings of this study are available from the corresponding author upon request.

Acknowledgments: The authors thank Joaquim Agostinho Gomes Moreira and Abílio de Jesus Monteiro Almeida for providing the research laboratories and their supervision likewise CNPq, FAPEAM, and CAPES; Postdoctoral National Program (PNPD/CAPES), Edital No. 047/2016–PPGFIS/UFAM. Fundação para a Ciência e Tecnologia (FCT) project CERN/FIS-TEC/0003/2019 and CQVR–UIDB/QUI/00616/2020. Project: NORTE-01-0145-FEDER-0000084.

Conflicts of Interest: The authors declare no conflict of interest. The funders had no role in the design analyses or interpretation of data; in the writing of the manuscript, or in the decision to publish the results.

References

1. Choi, T.; Horibe, Y.; Yi, H.T.; Choi, Y.J.; Wu, W.; Cheong, S.-W. Insulating interlocked ferroelectric and structural antiphase domain walls in multiferroic YMnO3. *Nat. Mater.* **2010**, *9*, 253–258. [CrossRef] [PubMed]
2. Lee, S.; Pirogov, A.; Kang, M.; Jang, K.-H.; Yonemura, M.; Kamiyama, T.; Cheong, S.-W.; Gozzo, F.; Shin, N.; Kimura, H.; et al. Giant magneto-elastic coupling in multiferroic hexagonal manganites. *Nature* **2008**, *451*, 805–808. [CrossRef]
3. Gajek, M.; Bibes, M.; Fusil, S.; Bouzehouane, K.; Fontcuberta, J.; Barthélémy, A.; Fert, A. Tunnel junctions with multiferroic barriers. *Nat. Mater.* **2007**, *6*, 296–302. [CrossRef]
4. Eerenstein, W.; Mathur, N.D.; Scott, J.F. Multiferroic and magnetoelectric materials. *Nature* **2006**, *442*, 759–765. [CrossRef] [PubMed]
5. Li, M.; Tan, H.; Duan, W. Hexagonal rare-earth manganites and ferrites: A review of improper ferroelectricity, magnetoelectric coupling, and unusual domain walls. *Phys. Chem. Chem. Phys.* **2020**, *22*, 14415–14432. [CrossRef] [PubMed]
6. Zhao, B.; Hu, X.; Dong, F.; Wang, Y.; Wang, H.; Tan, W.; Huo, D. The Magnetic Properties and Magnetocaloric Effect of $Pr_{0.7}Sr_{0.3}MnO_3$ Thin Film Grown on $SrTiO_3$ Substrate. *Materials* **2023**, *16*, 75. [CrossRef]
7. A Mota, D.; Barcelay, Y.R.; Tavares, P.; Chaves, M.R.; Almeida, A.; Oliveira, J.; Ferreira, W.S.; Moreira, J.A. Competing exchanges and spin–phonon coupling in $Eu_{1-x}RxMnO_3$ (R = Y, Lu). *J. Phys. Condens. Matter* **2013**, *25*, 235602. [CrossRef]
8. Moreira, J.A.; Almeida, A.; Ferreira, W.S.; Araújo, J.P.; Pereira, A.M.; Chaves, M.R.; Costa, M.M.R.; Khomchenko, V.A.; Kreisel, J.; Chernyshov, D.; et al. Strong magnetoelastic coupling in orthorhombic $Eu_{1-x}Y_xMnO_3$ manganite. *Phys. Rev. B* **2010**, *82*, 094418. [CrossRef]
9. Dong, S.; Liu, J.-M. Recent progress of multiferroic perovskite manganites. *Mod. Phys. Lett. B* **2012**, *26*, 1230004. [CrossRef]
10. Fiebig, M. Revival of the magnetoelectric effect. *J. Phys. D Appl. Phys.* **2005**, *38*, R123–R152. [CrossRef]
11. Cheong, S.-W.; Mostovoy, M. Multiferroics: A magnetic twist for ferroelectricity. *Nat. Mater.* **2007**, *6*, 13–20. [CrossRef]

12. Park, J.; Jeon, G.S.; Choi, H.-Y.; Lee, C.; Jo, W.; Bewley, R.; McEwen, K.A.; Perring, T.G. Magnetic ordering and spin-liquid state of $YMnO_3$. *Phys. Rev. B* **2003**, *68*, 104426. [CrossRef]
13. Issing, S.; Fuchs, F.; Ziereis, C.; Batke, E.; Pimenov, A.; Ivanov, Y.V.; Mukhin, A.A.; Geurts, J. Lattice dynamics of $Eu_{1-x}Y_xMnO_3$ ($0 \leq x \leq 0.5$). *Eur. Phys. J. B* **2010**, *73*, 353–360. [CrossRef]
14. Figueiras, F.G.; Karpinsky, D.; Tavares, P.B.; Gonçalves, J.N.; Yañez-Vilar, S.; Dos Santos, A.F.M.; Franz, A.; Tovar, M.; Moreira, J.A.; Amaral, V.S. Novel multiferroic state and ME enhancement by breaking the AFM frustration in $LuMn_{1-x}O_3$. *Phys. Chem. Chem. Phys.* **2017**, *19*, 1335–1341. [CrossRef] [PubMed]
15. Sergienko, I.A.; Şen, C.; Dagotto, E. Ferroelectricity in the MagneticE-Phase of Orthorhombic Perovskites. *Phys. Rev. Lett.* **2006**, *97*, 227204. [CrossRef] [PubMed]
16. Picozzi, S.; Yamauchi, K.; Sanyal, B.; Sergienko, I.; Dagotto, E. Dual Nature of Improper Ferroelectricity in a Magnetoelectric Multiferroic. *Phys. Rev. Lett.* **2007**, *99*, 227201. [CrossRef]
17. Meier, D.; Ryll, H.; Kiefer, K.; Klemke, B.; Hoffmann, J.-U.; Ramesh, R.; Fiebig, M. Mutual induction of magnetic 3dand 4forder in multiferroic hexagonal $ErMnO_3$. *Phys. Rev. B* **2012**, *86*, 184415. [CrossRef]
18. Liu, J.; Toulouse, C.; Rovillain, P.; Cazayous, M.; Gallais, Y.; Measson, M.-A.; Lee, N.; Cheong, S.W.; Sacuto, A. Lattice and spin excitations in multiferroich-YbMnO3. *Phys. Rev. B* **2012**, *86*, 184410. [CrossRef]
19. Goto, T.; Yamasaki, Y.; Watanabe, H.; Kimura, T.; Tokura, Y. Anticorrelation between ferromagnetism and ferroelectricity in perovskite manganites. *Phys. Rev. B* **2005**, *72*, 220403. [CrossRef]
20. Sergienko, I.A.; Dagotto, E. Role of the Dzyaloshinskii-Moriya interaction in multiferroic perovskites. *Phys. Rev. B* **2006**, *73*, 094434. [CrossRef]
21. Mochizuki, M.; Furukawa, N. Mechanism of Lattice-Distortion-Induced Electric-Polarization Flop in the Multiferroic Perovskite Manganites. *J. Phys. Soc. Jpn.* **2009**, *78*, 053704. [CrossRef]
22. Hemberger, J.; Schrettle, F.; Pimenov, A.; Lunkenheimer, P.; Ivanov, V.Y.; Mukhin, A.A.; Balbashov, A.M.; Loidl, A. Multiferroic phases of$Eu_{1-x}Y_xMnO_3$. *Phys. Rev. B* **2007**, *75*, 035118. [CrossRef]
23. Zheng, W.; Oitmaa, J.; Hamer, C.J. Phase diagram of the frustrated Heisenberg antiferromagnet on the union jack lattice. *Phys. Rev. B* **2007**, *75*, 184418. [CrossRef]
24. Takahashi, Y.; Yamasaki, Y.; Kida, N.; Kaneko, Y.; Arima, T.; Shimano, R.; Tokura, Y. Far-infrared optical study of electromagnons and their coupling to optical phonons in $Eu_{1-x}YxMnO_3$ (x = 0.1, 0.2, 0.3, 0.4, and 0.45). *Phys. Rev. B* **2009**, *79*, 214431. [CrossRef]
25. Moreira, J.A.; Almeida, A.; Ferreira, W.S.; Araújo, J.E.; Pereira, A.M.; Chaves, M.R.; Kreisel, J.; Vilela, S.M.F.; Tavares, P.B. Coupling between phonons and magnetic excitations in orthorhombic $Eu_{1-x}YxMnO_3$. *Phys. Rev. B* **2010**, *81*, 054447. [CrossRef]
26. Oliveira, J.; Moreira, J.A.; Almeida, A.; Chaves, M.R.; da Silva, J.M.M.; Sá, M.A.; Tavares, P.B.; Ranjith, R.; Prellier, W. Phase diagram of the orthorhombic, lightly lutetium doped EuMnO3magnetoelectric system. *Phys. Rev. B* **2011**, *84*, 094414. [CrossRef]
27. Romaguera-Barcelay, Y.; Moreira, J.A.; González-Aguilar, G.; Almeida, A.; Araujo, J.P.; De La Cruz, J.P. Synthesis of orthorhombic rare-earth manganite thin films by a novel chemical solution route. *J. Electroceramics* **2011**, *26*, 44–55. [CrossRef]
28. Barcelay, Y.R.; Moreira, J.A.; Almeida, A.; De La Cruz, J.P. Structural and electrical properties of LuMnO3 thin film prepared by chemical solution method. *Thin Solid Films* **2012**, *520*, 1734–1739. [CrossRef]
29. Kamiński, M.; Świta, P. Structural stability and reliability of the underground steel tanks with the Stochastic Finite Element Method. *Arch. Civ. Mech. Eng.* **2015**, *15*, 593–602. [CrossRef]
30. Van Aken, B.B.; Meetsma, A.; Palstra, T.T.M. Hexagonal $LuMnO_3$revisited. *Acta Crystallogr. Sect. E Struct. Rep. Online* **2001**, *57*, i101–i103. [CrossRef]
31. Abrahams, S.C. Ferroelectricity and structure in the $YMnO_3$ family. *Acta Crystallogr. Sect. B Struct. Sci.* **2001**, *57*, 485–490. [CrossRef] [PubMed]
32. Kimura, T.; Ishihara, S.; Shintani, H.; Arima, T.; Takahashi, K.T.; Ishizaka, K.; Tokura, Y. Distorted perovskite witheg1configuration as a frustrated spin system. *Phys. Rev. B* **2003**, *68*, 060403. [CrossRef]
33. Vailionis, A.; Boschker, H.; Siemons, W.; Houwman, E.P.; Blank, D.H.A.; Rijnders, G.; Koster, G. Misfit strain accommodation in epitaxialABO3perovskites: Lattice rotations and lattice modulations. *Phys. Rev. B* **2011**, *83*, 064101. [CrossRef]
34. Woodward, P.M.; Vogt, T.; Cox, D.E.; Arulraj, A.; Rao, C.N.R.; Karen, P.; Cheetham, A.K. Influence of Cation Size on the Structural Features of $Ln_{1/2}A_{1/2}MnO_3$ Perovskites at Room Temperature. *Chem. Mater.* **1998**, *10*, 3652–3665. [CrossRef]
35. Iliev, M.N.; Abrashev, M.V.; Laverdière, J.; Jandl, S.; Gospodinov, M.M.; Wang, Y.-Q.; Sun, Y.-Y. Distortion-dependent Raman spectra and mode mixing in RMnO3 perovskites (R = La, Pr, Nd, Sm, Eu, Gd, Tb, Dy, Ho, Y). *Phys. Rev. B* **2006**, *73*, 064302. [CrossRef]
36. Martín-Carrón, L.; de Andrés, A.; Martínez-Lope, M.J.; Casais, M.T.; Alonso, J.A. Raman phonons as a probe of disorder, fluctuations, and local structure in doped and undoped orthorhombic and rhombohedral manganites. *Phys. Rev. B* **2002**, *66*, 174303. [CrossRef]
37. Moreira, J.A.; Almeida, A.; Ferreira, W.; Chaves, M.; Oliveira, J.; da Silva, J.M.; Sá, M.; Vilela, S.; Tavares, P. Ferroelectricity in antiferromagnetic phases of $Eu_{1-x}Y_xMnO_3$. *Solid State Commun.* **2011**, *151*, 368–371. [CrossRef]

38. Figueiras, F.; Dutta, D.; Ferreira, N.; Costa, F.; Graça, M.; Valente, M. Multiferroic interfaces in bismuth ferrite composite fibers grown by laser floating zone technique. *Mater. Des.* **2016**, *90*, 829–833. [CrossRef]
39. Romaguera-Barcelay, Y.; Figueiras, F.; Moreira, J.A.; Pérez-De-La-Cruz, J.; Tavares, P.; Almeida, A. Handling magnetic and structural properties of $EuMnO_3$ thin films by the combined effect of Lu doping and substrate strain. *J. Alloy. Compd.* **2018**, *762*, 319–325. [CrossRef]

Disclaimer/Publisher's Note: The statements, opinions and data contained in all publications are solely those of the individual author(s) and contributor(s) and not of MDPI and/or the editor(s). MDPI and/or the editor(s) disclaim responsibility for any injury to people or property resulting from any ideas, methods, instructions or products referred to in the content.